CLNS 06/1980, CLEO 06-20

χ_{cJ} Decays to $h^+h^-h^0$

S. B. Athar,[1] R. Patel,[1] V. Potlia,[1] J. Yelton,[1] P. Rubin,[2] C. Cawlfield,[3] B. I. Eisenstein,[3] I. Karliner,[3] D. Kim,[3] N. Lowrey,[3] P. Naik,[3] M. Selen,[3] E. J. White,[3] J. Wiss,[3] R. E. Mitchell,[4] M. R. Shepherd,[4] D. Besson,[5] T. K. Pedlar,[6] D. Cronin-Hennessy,[7] K. Y. Gao,[7] J. Hietala,[7] Y. Kubota,[7] T. Klein,[7] B. W. Lang,[7] R. Poling,[7] A. W. Scott,[7] A. Smith,[7] P. Zweber,[7] S. Dobbs,[8] Z. Metreveli,[8] K. K. Seth,[8] A. Tomaradze,[8] J. Ernst,[9] K. M. Ecklund,[10] H. Severini,[11] W. Love,[12] V. Savinov,[12] O. Aquines,[13] Z. Li,[13] A. Lopez,[13] S. Mehrabyan,[13] H. Mendez,[13] J. Ramirez,[13] G. S. Huang,[14] D. H. Miller,[14] V. Pavlunin,[14] B. Sanghi,[14] I. P. J. Shipsey,[14] B. Xin,[14] G. S. Adams,[15] M. Anderson,[15] J. P. Cummings,[15] I. Danko,[15] D. Hu,[15] B. Moziak,[15] J. Napolitano,[15] Q. He,[16] J. Insler,[16] H. Muramatsu,[16] C. S. Park,[16] E. H. Thorndike,[16] F. Yang,[16] T. E. Coan,[17] Y. S. Gao,[17] M. Artuso,[18] S. Blusk,[18] J. Butt,[18] J. Li,[18] N. Menaa,[18] R. Mountain,[18] S. Nisar,[18] K. Randrianarivony,[18] R. Sia,[18] T. Skwarnicki,[18] S. Stone,[18] J. C. Wang,[18] K. Zhang,[18] G. Bonvicini,[19] D. Cinabro,[19] M. Dubrovin,[19] A. Lincoln,[19] D. M. Asner,[20] K. W. Edwards,[20] R. A. Briere,[21] T. Ferguson,[21] G. Tatishvili,[21] H. Vogel,[21] M. E. Watkins,[21] J. L. Rosner,[22] N. E. Adam,[23] J. P. Alexander,[23] D. G. Cassel,[23] J. E. Duboscq,[23] R. Ehrlich,[23] L. Fields,[23] L. Gibbons,[23] R. Gray,[23] S. W. Gray,[23] D. L. Hartill,[23] B. K. Heltsley,[23] D. Hertz,[23] C. D. Jones,[23] J. Kandaswamy,[23] D. L. Kreinick,[23] V. E. Kuznetsov,[23] H. Mahlke-Krüger,[23] P. U. E. Onyisi,[23] J. R. Patterson,[23] D. Peterson,[23] J. Pivarski,[23] D. Riley,[23] A. Ryd,[23] A. J. Sadoff,[23] H. Schwarthoff,[23] X. Shi,[23] S. Stroiney,[23] W. M. Sun,[23] T. Wilksen,[23] and M. Weinberger[23]

(CLEO Collaboration)

[1]*University of Florida, Gainesville, Florida 32611*
[2]*George Mason University, Fairfax, Virginia 22030*
[3]*University of Illinois, Urbana-Champaign, Illinois 61801*
[4]*Indiana University, Bloomington, Indiana 47405*
[5]*University of Kansas, Lawrence, Kansas 66045*
[6]*Luther College, Decorah, Iowa 52101*
[7]*University of Minnesota, Minneapolis, Minnesota 55455*
[8]*Northwestern University, Evanston, Illinois 60208*
[9]*State University of New York at Albany, Albany, New York 12222*
[10]*State University of New York at Buffalo, Buffalo, New York 14260*
[11]*University of Oklahoma, Norman, Oklahoma 73019*
[12]*University of Pittsburgh, Pittsburgh, Pennsylvania 15260*
[13]*University of Puerto Rico, Mayaguez, Puerto Rico 00681*
[14]*Purdue University, West Lafayette, Indiana 47907*
[15]*Rensselaer Polytechnic Institute, Troy, New York 12180*
[16]*University of Rochester, Rochester, New York 14627*
[17]*Southern Methodist University, Dallas, Texas 75275*
[18]*Syracuse University, Syracuse, New York 13244*
[19]*Wayne State University, Detroit, Michigan 48202*
[20]*Carleton University, Ottawa, Ontario, Canada K1S 5B6*
[21]*Carnegie Mellon University, Pittsburgh, Pennsylvania 15213*
[22]*Enrico Fermi Institute, University of Chicago, Chicago, Illinois 60637*

[23]*Cornell University, Ithaca, New York 14853*

(Dated: February 9, 2006)

Abstract

Using a sample of 3×10^6 $\psi(2S)$ decays recorded by the CLEO detector, we study three-body decays of the χ_{c0}, χ_{c1}, and χ_{c2} produced in radiative decays of the $\psi(2S)$. We consider the final states $\pi^+\pi^-\eta$, $K^+K^-\eta$, $p\bar{p}\eta$, $\pi^+\pi^-\eta'$, $K^+K^-\pi^0$, $p\bar{p}\pi^0$, $\pi^+K^-K^0_{\mathrm{S}}$, and $K^+\bar{p}\Lambda$, measuring branching fractions or placing upper limits. For $\chi_{c1} \to \pi^+\pi^-\eta$, $K^+K^-\pi^0$, and $\pi^+K^-K^0_{\mathrm{S}}$ our observed samples are large enough to indicate the largest contributions to the substructure.

I. INTRODUCTION

Decays of the χ_{c0}, χ_{c1}, and χ_{c2} states are not as well studied experimentally and theoretically as those of other charmonium states. These states have charge-conjugation eigenvalue $C = +1$, in contrast to the better-studied $C = -1$ states J/ψ and $\psi(2S)$. Their decay products thus will differ from those of J/ψ and $\psi(2S)$, and may provide complementary information on states containing light quarks and gluons. It is possible that the color-octet mechanism, $c\bar{c}g \to 2(q\bar{q})$, could have large effects on the observed decay pattern of the χ_{cJ} states [1]. Assuming that χ_{cJ} are the ${}^3P_J$ $c\bar{c}$ bound states one would expect that χ_{c0} and χ_{c2} with J^{PC} quantum numbers 0^{++} and 2^{++} decay to light quarks via two gluons [2]. Measurement of any possible χ_{cJ} hadronic decays provides valuable information on possible glueball dynamics. Thus knowledge of any hadronic decay channels for these states is valuable.

CLEO has gathered a large sample of $e^+e^- \to \psi(2S)$ events, which leads to copious production of the χ_{cJ} states in radiative decays of the $\psi(2S)$. The $\psi(2S)$ branching fractions have been recently measured [3] with high precision:

$$\mathcal{B}(\psi(2S) \to \gamma\chi_{c0}) = (9.22 \pm 0.11 \pm 0.46)\%; \quad (1)$$

$$\mathcal{B}(\psi(2S) \to \gamma\chi_{c1}) = (9.07 \pm 0.11 \pm 0.54)\%; \quad (2)$$

$$\mathcal{B}(\psi(2S) \to \gamma\chi_{c2}) = (9.33 \pm 0.14 \pm 0.61)\%. \quad (3)$$

We describe a study of selected three-body hadronic decay modes of the χ_{cJ} to two charged and one neutral hadron. This is not an exhaustive study of χ_{cJ} hadronic decays; we do not even comprehensively cover all possible $h^+h^-h^0$ decays, but simply take a first look at the rich structure of χ_{cJ} decays in our initial $\psi(2S)$ data sets. A subset of these modes has been investigated by BES [4]. With the CLEO III detector configuration [5], we have recorded an integrated luminosity of 2.57 pb^{-1} and the number of $\psi(2S)$ events is 1.56×10^6. With the CLEO-c detector configuration [6] we have recorded 2.89 pb^{-1}, and the number of events is 1.52×10^6. The apparent mis-match of luminosities and event totals is due to different beam energy spreads for the two data sets.

II. MEASUREMENT OF THE BRANCHING FRACTIONS

Our basic technique is an exclusive whole-event analysis searching for $\psi(2S) \to \gamma\chi_{cJ}$ followed by a three body decay of the χ_{cJ} to $\pi^+\pi^-\eta$, $K^+K^-\eta$, $p\bar{p}\eta$, $\pi^+\pi^-\eta'$, $K^+K^-\pi^0$, $p\bar{p}\pi^0$, $\pi^+K^-K^0_{\rm S}$, or $K^+\bar{p}\Lambda$. A photon candidate is combined with three hadrons and their 4-momentum sum constrained to the known total beam energy and the initial momentum caused by the two beams crossing at a small angle taking into account the measured errors on the reconstructed charged tracks, neutral hadron, and transition photon. We cut on the χ^2 of this fit, which has four degrees of freedom, as it strongly discriminates between background and signal. For most modes we select events with an event 4-momentum fit χ^2 less than 25, but background from $\psi(2S) \to J/\psi\pi^0\pi^0$ followed by charged two-body decays of the J/ψ, with one of the π^0 decay photons lost, fakes $\psi(2S) \to \gamma\chi_{cJ} \to \gamma p\bar{p}\pi^0$. For this mode the cut on χ^2 is tightened to 12. The efficiency of this cut is $\approx 95\%$ for all modes except $p\bar{p}\pi^0$, where it is $\approx 80\%$.

Efficiencies and backgrounds are studied in a GEANT-based simulation [7] of the detector response to $e^+e^- \to \psi(2S)$ events. Our simulated sample is roughly ten times our data sample. The radiated photon is generated according to an angular distribution of $1+\lambda\cos^2\theta$, where θ is the radiated photon angle relative to the positron beam axis. An E1 transition, as expected for $\psi(2S) \to \gamma\chi_{cJ}$, implies $\lambda = 1, -1/3, +1/13$ for $J = 0, 1, 2$ particles. The efficiencies we quote use this simulation, and differ from efficiencies using $\lambda = 0$ by up to a few percent.

Photon candidates are selected by their energy depositions in the CsI crystal calorimeter. They have a transverse shape consistent with that expected for an electromagnetic shower without a charged track pointing toward it. They are required to have an energy of at least 30 MeV. Photon candidates that are used to make neutral particles further must have an energy of more than 50 MeV if they are not in the barrel, $|\cos\theta_\gamma| > 0.82$, of our calorimeter. The $\pi^0 \to \gamma\gamma$ and $\eta \to \gamma\gamma$ candidates are formed from two-photon candidates that are kinematically fit to the known resonance masses using the event vertex position, determined using charged tracks constrained to the beam spot. We select events with a χ^2 from the kinematic mass fit with one degree of freedom of less than 10. Transition photon candidates are vetoed if they form a π^0 or η candidate when paired with a second photon candidate.

We also reconstruct the $\eta \to \pi^+\pi^-\pi^0$ mode combining two charged pions with a $\pi^0 \to \gamma\gamma$ candidate, increasing the number of η candidates by about 25%. The same sort of kinematic mass fit as used for π^0's and $\eta \to \gamma\gamma$ is applied to this mode, and again we select those giving a χ^2 of less than 10. Similarly we combine the mass-constrained η candidates together with two charged pions to make η' candidates, mass-constrain them, and select those with $\chi^2 < 10$. In addition, we include the decay mode $\eta' \to \gamma\rho$. Here the background is potentially high because of the large number of noise photons, so we require $E_{\rm photon} > 200$ MeV. In addition, we require the $\pi^+\pi^-$ mass to be within 100 MeV/c^2 of the mean ρ mass.

Charged tracks satisfy standard requirements [8] that they be of good fit quality. Those coming from the origin must have an impact parameter with respect to the beam spot less than the greater of $(5.0 - 3.8 \cdot p)$ mm and 1.2 mm, where p is the measured track momentum in GeV/c. The $K^0_S \to \pi^+\pi^-$ and $\Lambda \to p\pi^-$ candidates are formed from good-quality tracks that are constrained to come from a common vertex. The K^0_S flight path is required to be greater than 5 mm and the Λ flight path greater than 3 mm. The mass cut around the K^0_S mass is ± 10 MeV/c^2, and around the Λ mass ± 5 MeV/c^2, both about three times the resolution. Events with only the exact number of selected tracks are accepted. This selection is very efficient, >99.9%, for events passing all other requirements.

Pions are required to have specific ionization, dE/dx, in the main drift chamber within four standard deviations of the expected value for a real pion at the measured momentum. For kaons and protons, a combined dE/dx and RICH (ring imaging Cherenkov counter) likelihood is formed and kaons are required to be more kaon-like than pion- or proton-like, and similarly for protons. Cross feed between hadron species is negligible after all other requirements.

In modes comprising only two charged particles, there are some extra cuts to eliminate QED background which produce charged leptons in the final state. Events are rejected if the sum over all the charged tracks produces a penetration into the muon system of more than five nuclear interaction lengths. Events are rejected if any track has $0.92 < E/p < 1.05$ and it has a dE/dx consistent with an electron. This latter cut is not used for $p\bar{p}$ modes because anti-protons tend to deposit all their energy in the calorimeter. These cuts are essentially 100% efficient for the signal, and ensure this QED background is negligible.

The efficiencies averaged over the CLEO III and CLEO-c data sets for each mode including the branching fractions $\eta \to \gamma\gamma$, $\eta \to \pi^+\pi^-\pi^0$, and $\eta' \to \eta\pi^+\pi^-$ [9] are given in

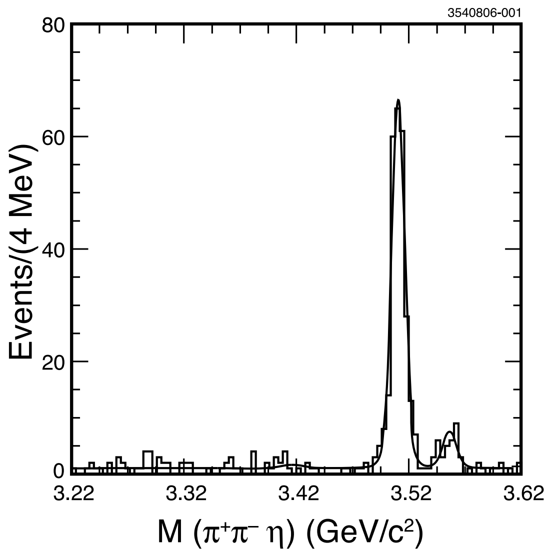

FIG. 1: Mass distribution for candidate $\chi_{cJ} \to \pi^+\pi^-\eta$ events. The displayed fit is described in the text.

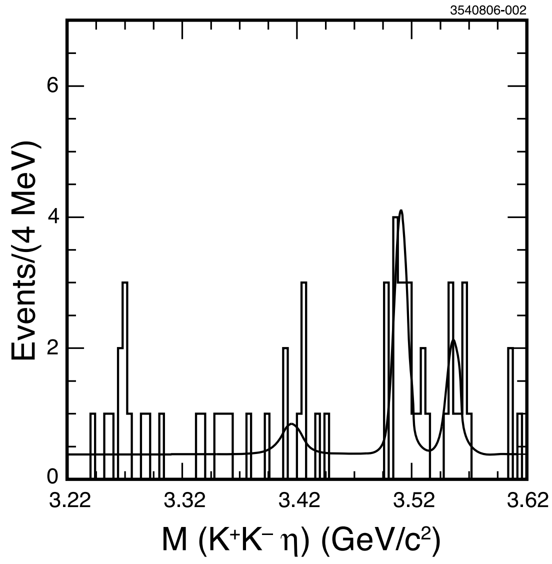

FIG. 2: Mass distribution for candidate $\chi_{cJ} \to K^+K^-\eta$ events. The displayed fit is described in the text.

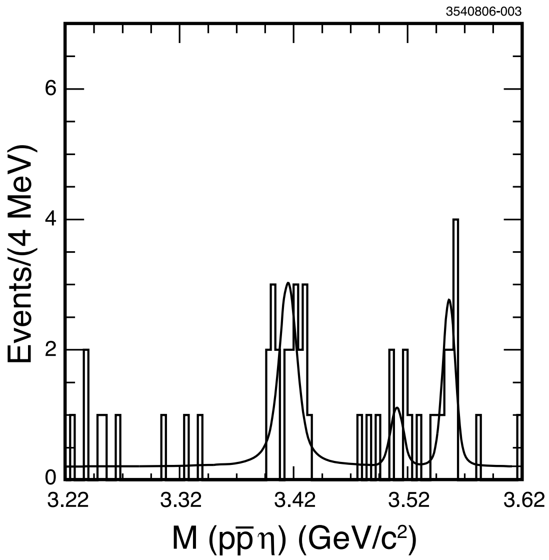

FIG. 3: Mass distribution for candidate $\chi_{cJ} \to p\bar{p}\eta$ events. The displayed fit is described in the text.

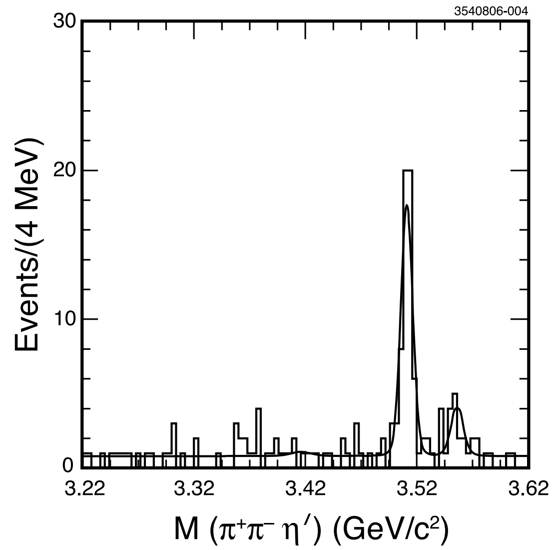

FIG. 4: Mass distribution for candidate $\chi_{cJ} \to \pi^+\pi^-\eta'$ events. The displayed fit is described in the text.

Tables I-III for χ_{c0}, χ_{c1}, and χ_{c2} respectively. Figures 1-8 show the mass distributions for the eight χ_{cJ} decay modes selected by the analysis described above. Signals are evident in all three χ_{cJ} states, but not in all the modes. Backgrounds are small. The mass distributions are fit to three signal shapes, Breit-Wigners convolved with Gaussian detector resolutions, and a linear background. The χ_{cJ} masses and intrinsic widths are fixed at the values from the Particle Data Group compilation [9]. The detector resolution is taken from the simulation discussed above. The simulation properly takes into account the amount of data in the two detector configurations, and the distribution of different decay modes we have observed.

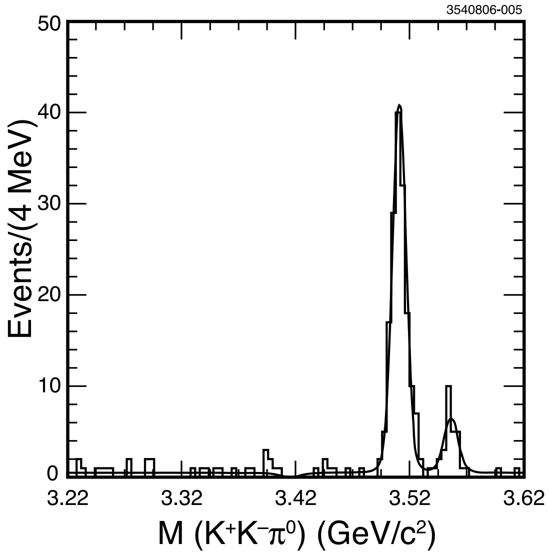

FIG. 5: Mass distribution for candidate $\chi_{cJ} \to K^+K^-\pi^0$ events. The displayed fit is described in the text.

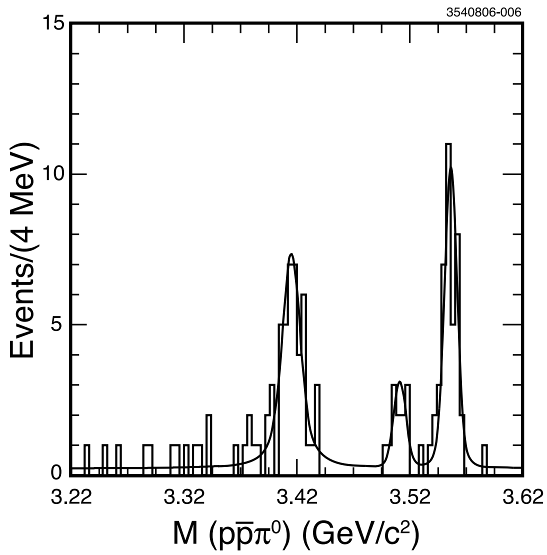

FIG. 6: Mass distribution for candidate $\chi_{cJ} \to p\bar{p}\pi^0$ events. The displayed fit is described in the text.

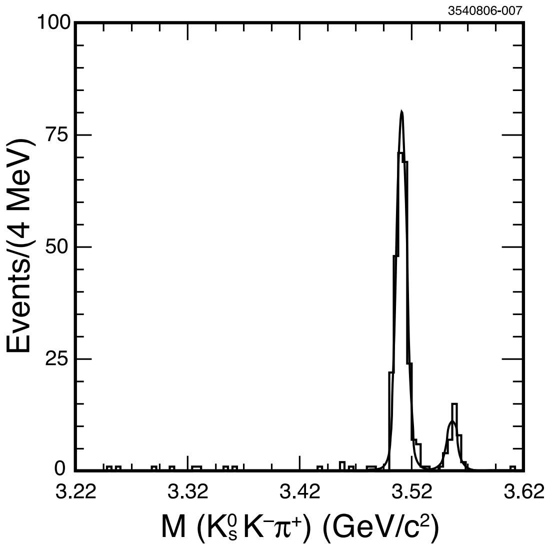

FIG. 7: Mass distribution for candidate $\chi_{cJ} \to K^0_S K^-\pi^+$ events. The displayed fit is described in the text.

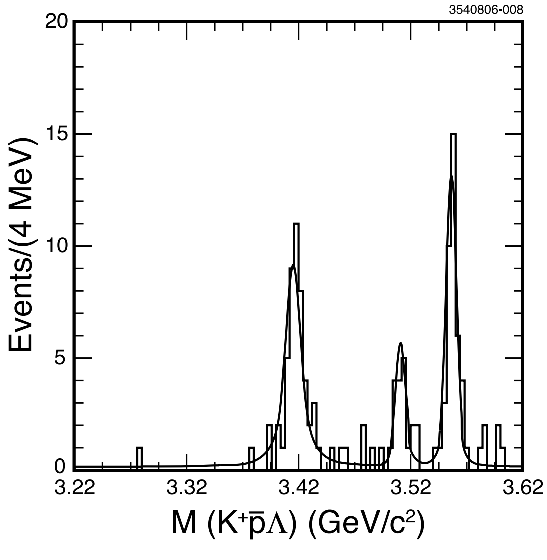

FIG. 8: Mass distribution for candidate $\chi_{cJ} \to K^+\bar{p}\Lambda$ events. The displayed fit is described in the text.

We approximate the resolution with a single Gaussian distribution, and variations are considered in the determination of systematic uncertainty. The detector resolution dominates for the χ_{c1} and χ_{c2}, but is similar to the intrinsic width of the χ_{c0}. The fits are displayed in Figures 1-8 and summarized in Tables I-III. Note that for the χ_{c0} in Table I the five modes for which no significant signal is found (yield less than three standard deviations from zero) are forbidden by parity conservation.

We consider various sources of systematic uncertainties on the yields. We varied the fitting procedure by allowing the χ_{cJ} masses and intrinsic widths to float. The fitted masses and

TABLE I: Parameters used and results of fits to the χ_{cJ} mass distributions of Figures 1-8 for the χ_{c0} signal. The fit is described in the text and the yield error is only statistical. If no significant signal is observed we also show an upper limit at 90% confidence level.

Mode	Efficiency (%)	Resolution (MeV)	Yield
$\pi^+\pi^-\eta$	18.2	6.23	4.2 ± 4.1 (< 10.6)
$K^+K^-\eta$	13.8	6.10	3.1 ± 2.7 (< 9.3)
$p\bar{p}\eta$	16.1	5.42	$17.7^{+5.2}_{-4.8}$
$\pi^+\pi^-\eta'$	8.0	4.38	2.0 ± 3.8 (< 8.5)
$K^+K^-\pi^0$	27.6	6.47	-3.3 ± 2.7 (< 4.7)
$p\bar{p}\pi^0$	27.8	5.80	$46.4^{+8.0}_{-7.2}$
$\pi^+K^-K^0_S$	19.8	4.75	0.0 ± 1.0 (< 2.7)
$K^+\bar{p}\Lambda$	16.8	4.38	$51.3^{+8.1}_{-7.4}$

TABLE II: Parameters used and results of fits to the χ_{cJ} mass distributions of Figures 1-8 for the χ_{c1} signal. The fit is described in the text and the yield error is only statistical. If no significant signal is observed we also show an upper limit at 90% confidence level.

Mode	Efficiency (%)	Resolution (MeV)	Yield
$\pi^+\pi^-\eta$	18.8	5.85	255^{+17}_{-16}
$K^+K^-\eta$	14.6	5.66	$14.1^{+4.6}_{-3.9}$
$p\bar{p}\eta$	17.7	5.41	3.2 ± 2.3 (< 7.6)
$\pi^+\pi^-\eta'$	8.5	4.37	$57.6^{+8.4}_{-7.7}$
$K^+K^-\pi^0$	29.2	6.79	157 ± 13
$p\bar{p}\pi^0$	30.1	5.23	$9.9^{+3.8}_{-3.2}$
$\pi^+K^-K^0_S$	20.6	4.37	249 ± 16
$K^+\bar{p}\Lambda$	17.7	4.38	$16.3^{+4.7}_{-4.0}$

widths agree with the values from the Particle Data Group [9], and we take the maximum variation in the observed yields, $\pm 4\%$, as a systematic uncertainty from the fit procedure. Allowing a curvature term to the background has a negligible effect. For modes with large yields we can break up the sample into CLEO III and CLEO-c data sets, and fit with resolutions and efficiencies appropriate for the individual data sets. We note that the separate data sets give consistent efficiency-corrected yields and the summed yield differs by 2% from the standard procedure, which is small compared to the $\pm 8\%$ statistical uncertainty. We take this as the systematic uncertainty from our resolution model. From studies of other processes we assign a $\pm 0.7\%$ uncertainty for the efficiency of finding each charged track, $\pm 4.0\%$ for the $\gamma\gamma$ resonances, $\pm 2.0\%$ for each extra photon, $\pm 1.3\%$ for the particle identification for each K and p, $\pm 2.0\%$ for secondary vertex finding, and $\pm 3.0\%$ from the statistical uncertainty on the efficiency determined from the simulation. We study the cut on the χ^2 of the event 4-momentum kinematic fit in the three large yield χ_{c1} signals by removing the χ^2 cut, selecting events around the χ_{c1} mass peak, subtracting a low-mass side band, the only one available, and comparing the simulated χ^2 distribution for signal events with the data distribution. This comparison is shown in Figure 9. The agreement between the data and simulation is good, and comparing the inefficiency introduced by our cut on the 4-momentum kinematic fit χ^2 between the data and the simulation we assign a $\pm 3.5\%$ uncertainty on the

TABLE III: Parameters used and results of fits to the χ_{cJ} mass distributions of Figures 1-8 for the χ_{c2} signal. The fit is described in the text and the yield error is only statistical. If no significant signal is observed we also show an upper limit at 90% confidence level.

Mode	Efficiency (%)	Resolution (MeV)	Yield
$\pi^+\pi^-\eta$	18.5	5.58	$26.2^{+6.4}_{-5.7}$
$K^+K^-\eta$	14.6	5.53	6.9 ± 2.9 (< 12.5)
$p\bar{p}\eta$	17.2	5.08	$9.5^{+3.8}_{-3.0}$
$\pi^+\pi^-\eta'$	8.5	4.32	$12.4^{+4.8}_{-4.1}$
$K^+K^-\pi^0$	27.5	6.85	$24.8^{+5.8}_{-5.1}$
$p\bar{p}\pi^0$	29.3	5.10	$37.1^{+6.7}_{-6.1}$
$\pi^+K^-K^0_S$	20.2	4.45	$36.8^{+6.6}_{-5.9}$
$K^+\bar{p}\Lambda$	17.5	4.32	$42.1^{+7.2}_{-6.5}$

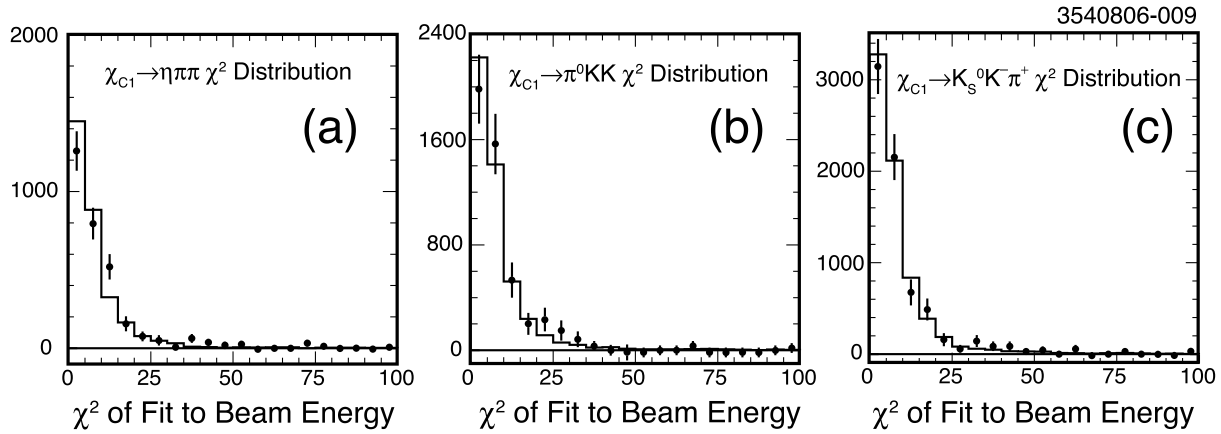

FIG. 9: Distribution of the χ^2 for the event 4-momentum kinematic fit shown here with a χ_{c1} mass cut and sideband subtraction. Plot (a) is the $\pi^+\pi^-\eta$ mode, (b) is the $K^+K^-\pi^0$ mode, and (c) is the $\pi^+K^-K^0_S$ mode. The data are shown by points and the simulation of signal events is shown by the solid line normalized to have the same area.

efficiency due to uncertainty in modeling this χ^2 distribution. The simulation was generated assuming three-body phase-space for the χ_{cJ} decay products. Deviations from this are to be expected. Based on the results of the Dalitz plot analyses discussed below we correct the efficiency in the $\chi_{c1} \to \pi^+\pi^-\eta$, $\chi_{c1} \to K^+K^-\pi^0$, and $\chi_{c1} \to K^-\pi^+K^0_S$ modes by a relative -2.2%, -1.5%, and $+6\%$ respectively to account for the change in the efficiency caused by the deviation from a uniform phase space distribution of decay products to what we actually observe. We apply an additional $\pm5\%$ uncertainty on all other modes to account for the effect of resonant sub-structure on the efficiency. The total systematic uncertainty is mode dependent, but is roughly 10%; it is higher for modes with many photons in the final state and lower for those with only one.

To calculate χ_{cJ} branching fractions, we use previous CLEO measurements for the $\psi(2S) \to \gamma\chi_{cJ}$ branching fractions from Equations 1-3 [3]. The uncertainties on these branching fractions are included in the systematic uncertainty on the χ_{cJ} branching fractions we report. Also there is a 3% uncertainty on the number of $\psi(2S)$ produced. Results for the three-body branching fractions are shown in Table IV. Where the yields do not show

TABLE IV: Branching fractions in units of 10^{-3}. Uncertainties are statistical, systematic due to detector effects plus analysis methods, and a separate systematic due to uncertainties in the $\psi(2S)$ branching fractions. Limits are at the 90% confidence level.

Mode	χ_{c0}	χ_{c1}	χ_{c2}
$\pi^+\pi^-\eta$	< 0.21	$5.0 \pm 0.3 \pm 0.4 \pm 0.3$	$0.49 \pm 0.12 \pm 0.05 \pm 0.03$
$K^+K^-\eta$	< 0.24	$0.34 \pm 0.10 \pm 0.03 \pm 0.02$	< 0.33
$p\bar{p}\eta$	$0.39 \pm 0.11 \pm 0.04 \pm 0.02$	< 0.16	$0.19 \pm 0.07 \pm 0.02 \pm 0.01$
$\pi^+\pi^-\eta'$	< 0.38	$2.4 \pm 0.4 \pm 0.2 \pm 0.2$	$0.51 \pm 0.18 \pm 0.05 \pm 0.03$
$K^+K^-\pi^0$	< 0.06	$1.95 \pm 0.16 \pm 0.18 \pm 0.14$	$0.31 \pm 0.07 \pm 0.03 \pm 0.02$
$p\bar{p}\pi^0$	$0.59 \pm 0.10 \pm 0.07 \pm 0.03$	$0.12 \pm 0.05 \pm 0.01 \pm 0.01$	$0.44 \pm 0.08 \pm 0.04 \pm 0.03$
$\pi^+K^-\overline{K}^0$	< 0.10	$8.1 \pm 0.6 \pm 0.6 \pm 0.5$	$1.3 \pm 0.2 \pm 0.1 \pm 0.1$
$K^+\bar{p}\Lambda$	$1.07 \pm 0.17 \pm 0.10 \pm 0.06$	$0.33 \pm 0.09 \pm 0.03 \pm 0.02$	$0.85 \pm 0.14 \pm 0.08 \pm 0.06$

clear signals we calculate 90% confidence level upper limits using the yield central values with the statistical errors from the yield fits combined in quadrature with the systematic uncertainties on the efficiencies and other branching fractions. We assume the uncertainty is distributed as a Gaussian and the upper limit is the branching fraction value at which 90% of the integrated area of the Gaussian falls below. We exclude the unphysical region, negative branching fractions, for this upper limit calculation. We note that the ratio of rates obtained from isospin symmetry (see Appendix VI, Equations 23 and 31), expected to be 4.0, is consistent with our measurement:

$$\frac{\Gamma(\chi_{c1} \to \pi^+K^-K^0) + \Gamma(\chi_{c1} \to \pi^-K^+\overline{K}^0)}{\Gamma(\chi_{c1} \to K^+K^-\pi^0)} = 4.2 \pm 0.7. \tag{4}$$

Our results are consistent with branching fractions and upper limits in the $\pi^+K^-K^0_S$ and $\pi^+\pi^-\eta$ modes from BES [4], but more precise.

III. SUBSTRUCTURE ANALYSIS

We perform a Dalitz plot analysis on the modes with the highest statistics, $\chi_{c1} \to \pi^+\pi^-\eta$, $\chi_{c1} \to K^+K^-\pi^0$, and $\chi_{c1} \to \pi^+K^-K^0_S$, to study the two-body substructure. For the Dalitz analysis only those events within 10 MeV, roughly two standard deviations, of the observed χ_{c1} signal peak mean in the specific mode are accepted. For $\chi_{c1} \to \pi^+\pi^-\eta$ there are 228 events in this region and the signal fit finds 224.2 signal events and 5.1 combinatorial background. For $\chi_{c1} \to K^+K^-\pi^0$ there are 137 events accepted with the fit finding 137.8 signal and 2.4 background events, and for $\chi_{c1} \to \pi^+K^-K^0_S$, the numbers are 234 events, of which 233.2 are signal and 0.8 are background. In all cases the contribution from the tail of the χ_{c2} is less than one event.

An unbinned maximum likelihood fit is used in order to perform the Dalitz plot analysis [11]. In order to assess the fit quality we use an adaptive binning technique [12] and calculate a probability for Pearson statistics. Efficiencies are determined with simulated event samples for the χ_{c1} decay generated uniformly in phase space, and run through the analysis procedure described above. The efficiency across the Dalitz plots is fit to a two-dimensional polynomial of third order in the Dalitz plot variables. The fits are of good-quality and the efficiency is generally flat across the Dalitz plot.

When fitting the data small contributions from backgrounds are neglected. We are examining the $e^+e^- \to \psi(2S) \to \gamma\chi_{c1}$ process. In such a decay the χ_{c1} should be polarized. In principle a complete analysis would take into account the angle of the photon with respect to the e^+e^- beams' collision axis and decompose the χ_{c1} decay into its partial waves. We use a simple model to analyze our data sample which is adequate for seeing the largest contributions to the substructure in our small sample. We take the Dalitz plot matrix element $|\mathcal{M}|^2$ to be a sum of non-interfering resonances,

$$|\mathcal{M}|^2 = \sum_R |A_R|^2 \cdot \Omega_R^2. \tag{5}$$

The quantity $A_R(m)$ represents the amplitude of each resonance contribution with angular distributions Ω_R^2 taken from Ref. [10] as shown in Table V.

TABLE V: Angular distributions from Ref. [10] used in the present analysis. The notation follows the original publication. We assume the decay of a particle with spin J ($J = 1$ for χ_{c1} in our case) to the resonance R of spin j and a pseudoscalar particle with relative orbital momentum L. The angle θ is the resonance decay angle with respect to the pseudoscalar particle in the resonance's rest frame. The term $z^2 = \gamma_R^2 - 1$ is a relativistic correction factor, where γ_R is the resonance Lorentz factor in the χ_{c1} rest frame.

$J \to j + L$	Angular distribution, Ω_R^2
1→0+1	uniform
1→1+0	$1 + z^2 \cos^2\theta$
1→1+2	$1 + (3 + 4z^2)\cos^2\theta$
1→2+1	$(1 + z^2)[1 + 3\cos^2\theta + 9z^2(\cos^2\theta - 1/3)^2]$

Narrow resonances are described with a Breit-Wigner amplitude

$$A_R(m) = \frac{a_R}{m_R^2 - m^2 - im\Gamma_{R,\ \mathrm{total}}(m)}. \tag{6}$$

The a_R coefficients are fit parameters giving the amplitudes of the resonance with spin j- and mass-dependent width

$$m\Gamma_{R,\ \mathrm{total}}(m) = \sum_f \mathcal{B}(R \to f) \cdot m_R \Gamma_R \left(\frac{p}{p_R}\right)^{2j+1} \frac{m_R}{m}, \tag{7}$$

where the resonance mass m_R, width Γ_R, and branching ratio $\mathcal{B}(R \to f)$ into the final state f are taken from previous experiments [9]; p and p_R are the decay products' momenta in the resonance rest frame and its value at $m = m_R$. For the scalar resonance $a_0(980)$ we use a Flatté parameterization in the style of the Crystal Barrel Collaboration [13],

$$A_{a_0(980)}(m) = \frac{a_{a_0(980)}}{m_R^2 - m^2 - i[g_{\eta\pi}^2 \rho_{\eta\pi}(m) + g_{\bar{K}K}^2 \rho_{\bar{K}K}(m)]}, \tag{8}$$

where m_R, $g_{\eta\pi}$, and $g_{\bar{K}K}$ are the resonance mass and coupling constants, m is the invariant mass of the resonance final state, and $\rho_{ab}(m)$ is a phase space factor for the particular final

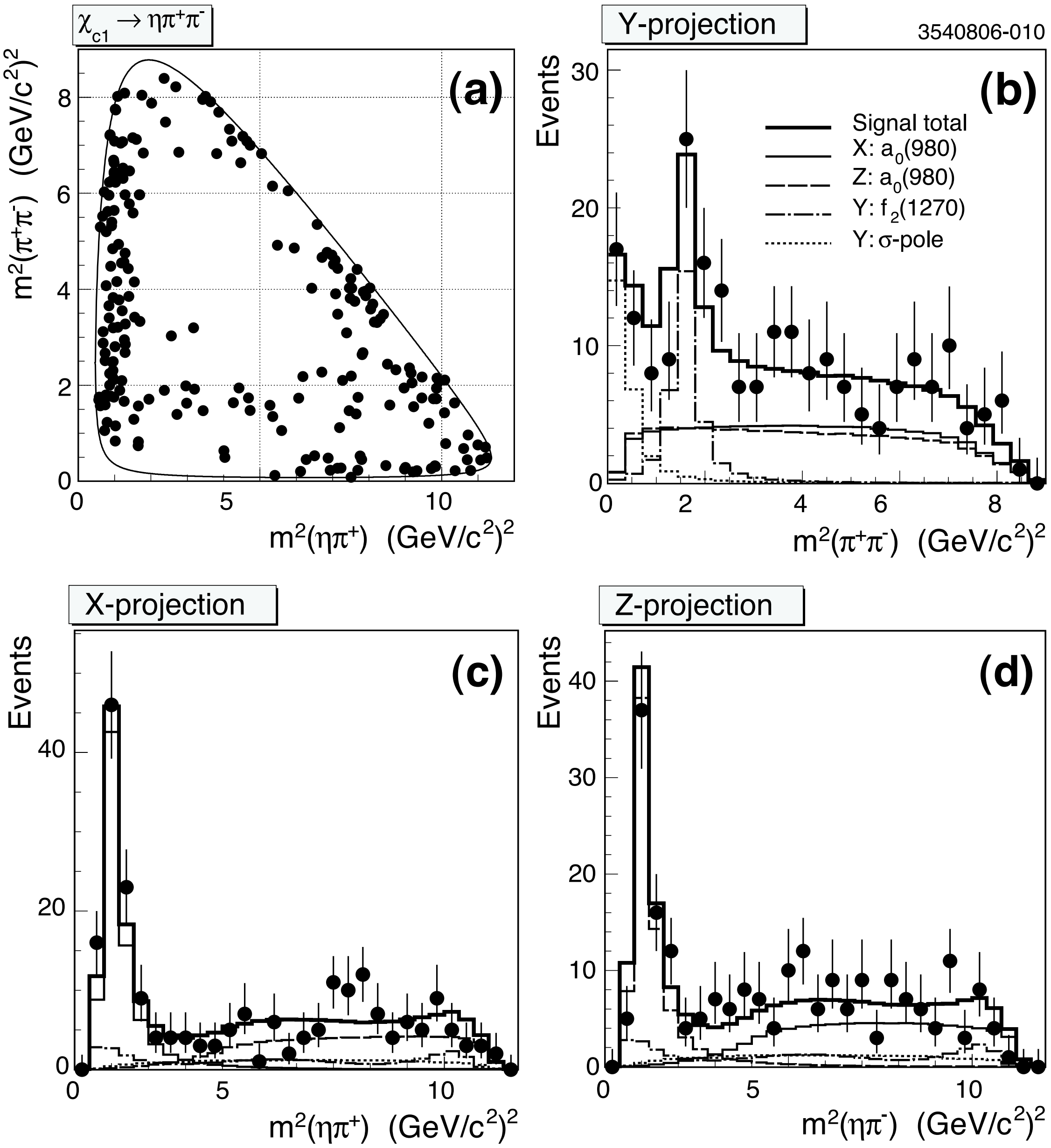

FIG. 10: (a) Dalitz plot, (b)–(d) projections on the three mass squared combinations for $\chi_{c1} \to \pi^+\pi^-\eta$. The displayed fit projections are described in the text.

state. We use the $a_0(980)$ line-shape parameters from Table VI. Similar details of the $f_0(980)$ parameterization are unimportant as it is used only in systematic studies.

For low-mass $\pi^+\pi^-(\sigma)$ and $K\pi(\kappa)$ S-wave contributions we choose a parameterization with a complex pole m_R [14],

$$A_R(m) = \frac{a_R}{m_R^2 - m^2}, \tag{9}$$

with $m_\sigma = (470 - i220)$ MeV and $m_\kappa = (710 - i310)$ MeV, which is adequate for our small sample.

Figure 10 shows the Dalitz plot and three projections for $\chi_{c1} \to \pi^+\pi^-\eta$. There are clear contributions from $a_0(980)^\pm\pi^\mp$ and $f_2(1270)\eta$ intermediate states, and significant accumulation of events at low $\pi^+\pi^-$ mass. Note that the $a_0(980)$ can contribute in two decay modes to the Dalitz plot. An isospin Clebsch-Gordan decomposition for this decay, given in Appendix VI, Equation 24, shows that amplitudes and strong phases of both charge-conjugated states should be equal. The overall amplitude normalization is arbitrary and we set $a_{a_0(980)^+} = a_{a_0(980)^-} = 1$. All other fit components are defined relative to this choice.

Our initial fit to this mode includes only $a_0(980)^\pm\pi^\mp$ and $f_2(1270)\eta$ contributions, but has a vanishing probability of 0.1% for describing the data due to the accumulation of events at low $\pi^+\pi^-$ mass. To account for this we try K^0_S, $f_0(980)$, $\rho(770)$, and σ resonances. Only the $\rho(770)$ and the σ give high fit probability. However the decay $\chi_{c1} \to \rho(770)\eta$ is C-forbidden, and the low-mass distribution is not well represented by the $\rho(770)$, which only gives an acceptable fit due to its large width and the limited statistics of our sample. The σ describes well the low $\pi^+\pi^-$ mass spectrum, and we describe the Dalitz plot with $a_0(980)^\pm\pi^\mp$, $f_2(1270)\eta$, and $\sigma\eta$ contributions. Table VII gives the results of this fit, which has a probability to match the data of 66%. The angular distributions for $a_0(980)^\pm$ and σ meson decays are uniform, and for $f_2(1270)$ are taken from Table V for quantum numbers $JjL = 121$. We assume that a possible contribution from $L = 3$ is small and it is neglected.

The systematic uncertainties shown in the table were obtained from variations to this

TABLE VI: Resonance parameters in the $\chi_{c1} \to \eta\pi^+\pi^-$ mode comparing their nominal value to fit values when individual resonance parameters are allowed to float.

Parameter	Nominal Value	When Floating
$m(a_0(980))$, MeV/c^2	999	1002±18
$g_{\eta\pi}$, MeV/c^2	620	637±49
$g_{K\bar{K}}$, MeV/c^2	500	523±154
Re(m_σ), MeV/c^2	470	511±28
Im(m_σ), MeV/c^2	–220	–102±50

nominal fit as discussed below. We allow the 2D-efficiency to vary with its polynomial coefficients constrained by the results of the fit to the simulated events; the mass of the $a_0(980)$ and its coupling constants are allowed to float, the parameters of the σ-pole are allowed to float, and we allow additional contributions from $\rho(770)\eta$, $f_0(980)\eta$, $K^0_S\eta$, and $\pi_1(1400)\pi$. The results of allowing the resonance parameters to float as compared to their fixed values used in the nominal fit are shown in Table VI. For the additional contributions we do not observe amplitudes that are significant and we limit their individual fit fractions

TABLE VII: Fit results for $\chi_{c1} \to \eta\pi^+\pi^-$ Dalitz plot analysis. The uncertainties are statistical and systematic. Allowing for interference among the resonances changes the fit fractions by as much as 20% in absolute terms as discussed in the text.

Mode	a_R	Fit Fraction (%)
$a_0(980)^\pm\pi^\mp$	1	$75.1 \pm 3.5 \pm 4.3$
$f_2(1270)\eta$	$0.103 \pm 0.014 \pm 0.005$	$14.4 \pm 3.1 \pm 1.9$
$\sigma\eta$	$0.41 \pm 0.05 \pm 0.10$	$10.5 \pm 2.4 \pm 1.2$

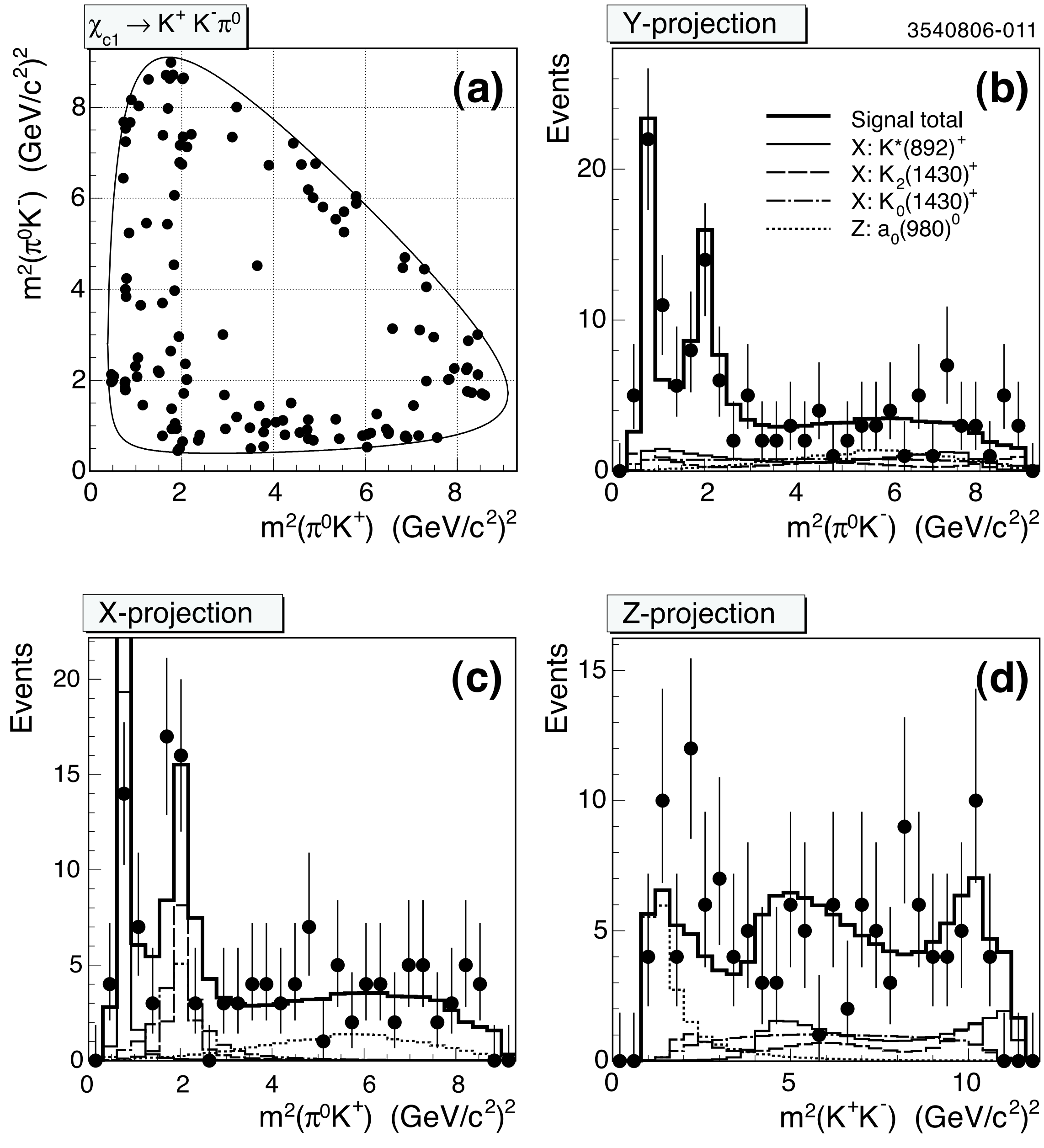

FIG. 11: (a) Dalitz plot, (b)–(d) projections on the three mass squared combinations for $\chi_{c1} \to K^+K^-\pi^0$. The displayed fit projections are described in the text. The contribution from π^0K^- resonances are not shown. They look similar to the π^0K^+ resonance components for the relevant projections.

to roughly less than 5% of the Dalitz plot. We note that with higher statistics this mode may offer one of the best measurements of the parameters of the $a_0(980)$. These results are consistent with the substructure analysis of this mode by BES [4].

The Dalitz plot for $\chi_{c1} \to K^+K^-\pi^0$ decay and its projections are shown in Figure 11, and for $\chi_{c1} \to \pi^+K^-K^0_S$ in Figure 12. We do a combined Dalitz plot analysis to these modes taking advantage of isospin symmetry. An isospin Clebsch-Gordan decomposition for these decays, described in Appendix VI, shows that these two Dalitz plots should have the same

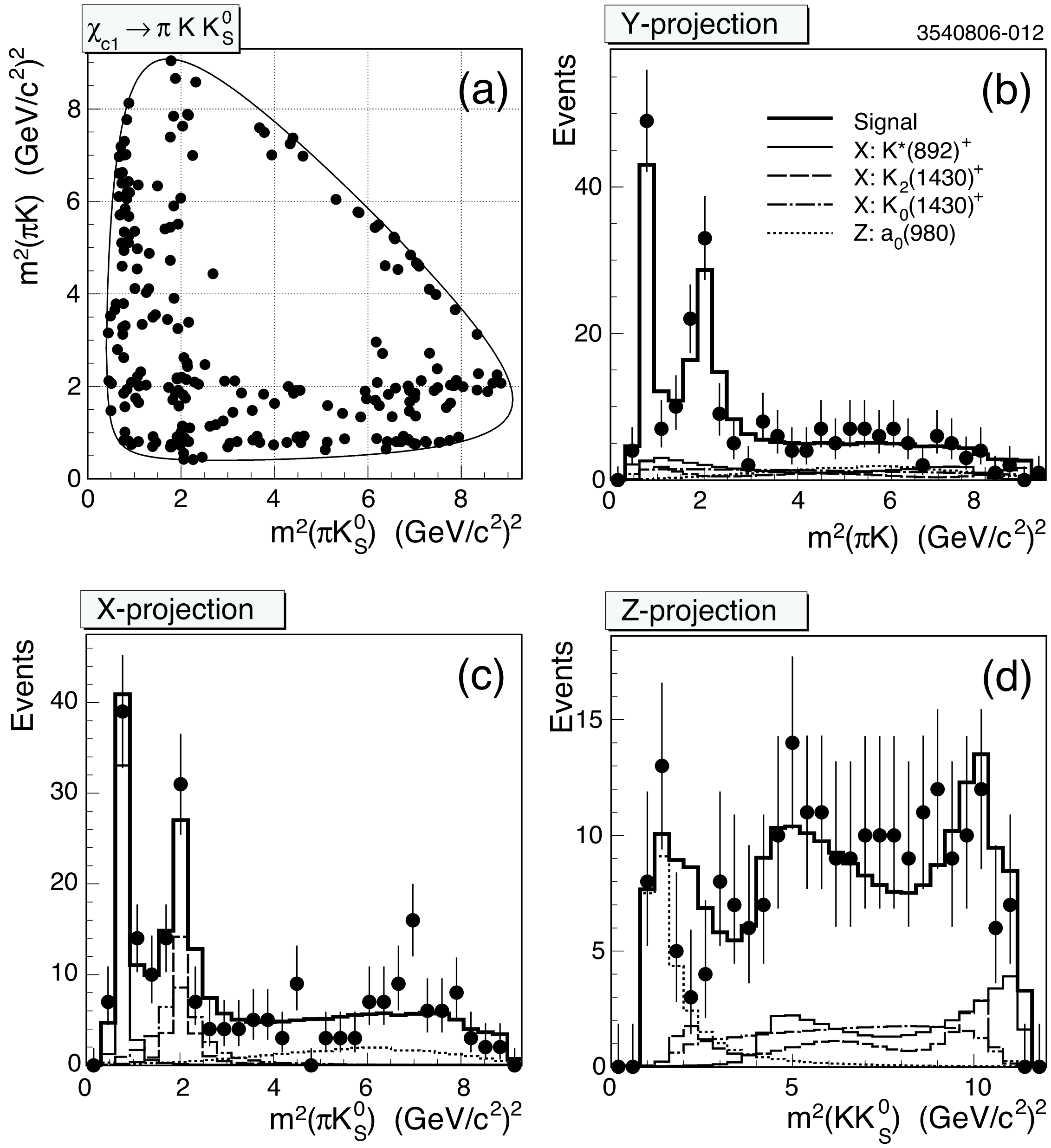

FIG. 12: (a) Dalitz plot, (b)–(d) projections on the three mass squared combinations for $\chi_{c1} \to \pi^+K^-K^0_S$. The displayed fit projections are described in the text. The π^+K^- resonances are not shown. They look similar to the $\pi^+K^0_S$ resonance components for the relevant projections.

set of amplitudes for all $K^*\overline{K}$ and $a_0(980)\pi$ intermediate states. The relative factor $-\sqrt{2}$ between the two Dalitz plot amplitudes does not matter due to the individual normalization of their probability density functions. In the combined fit to these two Dalitz plots, we use the following constraints on the amplitudes: $a_{K^*} \equiv a_{K^{*+}} = a_{K^{*-}} = a_{K^{*0}} = a_{\overline{K}^{*0}}$, and $a_{a(980)} \equiv a_{a(980)^+} = a_{a(980)^-} = a_{a(980)^0}$. The overall amplitude normalization is arbitrary and we set $a_{K^*(892)} = 1$.

Visual inspection shows apparent contributions from $K^*(892)^\pm K^\mp$, $K^*(892)^0K^0_S$, $K^*(1430)^\pm K^\mp$, $K^*(1430)^0K^0_S$, $a_0(980)^0\pi^0$, and $a_0(980)^\pm\pi^\mp$. It is not clear if the $K^*(1430)$

are K_0^* or K_2^*, and many other $K\pi$ and KK resonances can possibly contribute. The angular distribution for scalar resonance decays is always taken as uniform. The shape for $K^*(892)K$ is taken from Table V for quantum numbers $JjL = 110$. We also modeled this contribution with the $JjL = 112$ angular distribution with the difference taken as a systematic uncertainty. The shape for $K_2^*(1430)K$ is taken for quantum numbers $JjL = 121$, with a possible contribution from $L = 3$ ignored. Our best fit result is shown in Table VIII, displaying statistical and systematic errors. This fit has a good probability of matching the data,

TABLE VIII: Results of the combined fits to the $\chi_{c1} \to K^+K^-\pi^0$ and $\chi_{c1} \to \pi K K_S^0$ Dalitz plots. Allowing for interference among the resonances changes the fit fractions by as much as 15% in absolute terms as discussed in the text.

Mode	a_R	Fit Fraction (%)
$K^*(892)K$	1	$31.4 \pm 2.2 \pm 1.7$
$K_0^*(1430)K$	$3.8 \pm 0.4 \pm 0.2$	$30.4 \pm 3.5 \pm 3.7$
$K_2^*(1430)K$	$0.44 \pm 0.06 \pm 0.04$	$23.1 \pm 3.4 \pm 7.1$
$a_0(980)\pi$	$6.1 \pm 0.6 \pm 0.6$	$15.1 \pm 2.7 \pm 1.5$

73%, and agrees with fits done to the separate Dalitz plots not taking advantage of isospin symmetry. The addition of a κK contribution does not improve the fit probability and the amplitude a_κ is statistically significant only at the four standard deviation level. Similar behavior is noted for a non-resonant contribution. Systematic uncertainties are evaluated by observing deviations from the nominal fit as described above for the $\chi_{c1} \to \pi^+\pi^-\eta$ analysis. When systematics are taken into account neither the κK nor non-resonant contribution has a fit fraction significant at the three standard deviation level. Their individual contributions are limited to less than roughly 10% of the Dalitz plot. These observations are consistent with those by BES [4] in the $\pi^+K^-K_S^0$ mode.

While this model of the contributions to the Dalitz plots gives a good description of the data it is clearly incomplete. There should be interference among the resonances, which the simple approach of Equation 5 does not take into account. To quantify the effect of interference we have repeated the Dalitz analyses using a "quasi-coherent" (note that Ω_R^2 is always positively-defined) sum of amplitudes with floating complex weighting factors instead of a_R. This causes the fit fractions to change by as much as $\sim$20% absolutely in the $\eta\pi\pi$ analysis and $\sim$15% absolutely in the $K\overline{K}\pi$ analysis. With more data a study of the χ_{c1} decay substructure taking into account the effect of χ_{c1} polarization, using the orientation of the χ_{c1} decay plane with respect to the χ_{c1} flight direction, in a partial wave analysis would be a complete description of these decays. The matrix element amplitudes should include the partial wave dependent angular distributions and interference effects among the resonances. See Ref. [15] for appropriate prescriptions.

IV. SUMMARY

We have searched for and studied selected three-body hadronic decays of the χ_{c0}, χ_{c1}, and χ_{c2} produced in radiative decays of the $\psi(2S)$ in e^+e^- collisions observed with the CLEO detector. Many of the channels covered in this analyses are observed or limited for the first time. Our observations and branching fraction limits are summarized in Table IV. In $\chi_{c1} \to \pi^+\pi^-\eta$ we have studied the resonant substructure using a Dalitz plot analysis simply modeling the resonance contributions as non-interfering amplitudes. Our results are summarized in Table VII. We observe clear signals for the $a_0(980)^{\pm}\pi^{\mp}$ and $f_2(1270)\eta$ intermediate states, and a low-mass $\pi^+\pi^-$ enhancement. Similarly for $\chi_{c1} \to K\overline{K}\pi$ our results are summarized in Table VIII, assuming, based on isospin, that the $\pi K K^0_S$ and $K^+K^-\pi^0$ plots are identical. We observe $K^*(892)K$, $K^*_2(1430)K$ and likely $a_0(980)\pi$ contributions in the $K\overline{K}\pi$ Dalitz plots. Other conclusions about S-wave contributions are likely model-dependent.

V. ACKNOWLEDGMENTS

We gratefully acknowledge the effort of the CESR staff in providing us with excellent luminosity and running conditions. D. Cronin-Hennessy and A. Ryd thank the A.P. Sloan Foundation. This work was supported by the National Science Foundation, the U.S. Department of Energy, and the Natural Sciences and Engineering Research Council of Canada.

VI. APPENDIX: CLEBSCH-GORDAN DECOMPOSITION FOR χ_{c1}

In order to constrain amplitudes and phases in χ_{c1} decays we use a Clebsch-Gordan decomposition of the χ_{c1} (the state with $|I = 0, I_Z = 0\rangle$) for possible isospin subsystems:

$$\chi_{c1} \to (K\pi)_{I=1/2}\overline{K}, \tag{10}$$

$$\chi_{c1} \to (\overline{K}\pi)_{I=1/2}K, \tag{11}$$

$$\chi_{c1} \to (K\overline{K})_{I=1}\pi. \tag{12}$$

Below we use the Clebsch-Gordan decomposition rules, $|J, M\rangle = \sum_f c_f |m_1, m_2\rangle_f$ from Ref. [9].

A. Clebsch-Gordan decomposition for $K^* \to K\pi$ decays

We assume that K^* mesons with I=1/2 form two isodoublets: (K^{*+}, K^{*0}) and ($\overline{K}^{*0}$, K^{*-}) with ($I_Z = \frac{1}{2}$,$I_Z = -\frac{1}{2}$) respectively. The Clebsch-Gordan decomposition rules for $\mathbf{1} \times \frac{\mathbf{1}}{\mathbf{2}}$ isospin states are:

$$K^{*+} = \sqrt{\frac{2}{3}}\pi^+K^0 - \sqrt{\frac{1}{3}}\pi^0K^+, \tag{13}$$

$$K^{*0} = \sqrt{\frac{1}{3}}\pi^0K^0 - \sqrt{\frac{2}{3}}\pi^-K^+, \tag{14}$$

$$\overline{K}^{*0} = \sqrt{\frac{2}{3}}\pi^+K^- - \sqrt{\frac{1}{3}}\pi^0\overline{K}^0, \tag{15}$$

$$K^{*-} = \sqrt{\frac{1}{3}}\pi^0K^- - \sqrt{\frac{2}{3}}\pi^-\overline{K}^0. \tag{16}$$

B. Cases of $\chi_{c1} \to (K\pi)_{I=1/2}\overline{K}$ and $\chi_{c1} \to (\overline{K}\pi)_{I=1/2}K$ decays

For $\chi_{c1} \to K^*\overline{K}$ and $\chi_{c1} \to \overline{K}^*K$ modes we use the $\frac{\mathbf{1}}{\mathbf{2}} \times \frac{\mathbf{1}}{\mathbf{2}}$ rule:

$$\chi_{c1} = \frac{1}{\sqrt{2}}(K^{*+}K^- - K^{*0}\overline{K}^0), \tag{17}$$

$$\chi_{c1} = \frac{1}{\sqrt{2}}(\overline{K}^{*0}K^0 - K^{*-}K^+). \tag{18}$$

Combining Equations 17 and 18 with Equations 13-16 we get

$$\chi_{c1}\sqrt{2} = \sqrt{\frac{2}{3}}\Big[(\pi^+K^0)K^- + (\pi^-K^+)\overline{K}^0\Big] - \sqrt{\frac{1}{3}}\Big[(\pi^0K^+)K^- + (\pi^0K^0)\overline{K}^0\Big], \tag{19}$$

$$\chi_{c1}\sqrt{2} = \sqrt{\frac{2}{3}}\Big[(\pi^+K^-)K^0 + (\pi^-\overline{K}^0)K^+\Big] - \sqrt{\frac{1}{3}}\Big[(\pi^0K^-)K^+ + (\pi^0\overline{K}^0)K^0\Big]. \tag{20}$$

Assuming charge symmetry the amplitudes in Equations 19 and 20 should be equal. From these equations we get the ratio of rates:

$$\Gamma(\chi_{c1} \to \pi^+K^-K^0)/\Gamma(\chi_{c1} \to K^+K^-\pi^0) = 2, \tag{21}$$

$$\Gamma(\chi_{c1} \to \pi^-K^+\overline{K}^0)/\Gamma(\chi_{c1} \to K^+K^-\pi^0) = 2, \tag{22}$$

or their sum

$$\Gamma(\chi_{c1} \to \pi^+K^-K^0) + \Gamma(\chi_{c1} \to \pi^-K^+\overline{K}^0) = 4 \cdot \Gamma(\chi_{c1} \to K^+K^-\pi^0). \tag{23}$$

C. Case of $\chi_{c1} \to (K\overline{K})_{I=1}\pi$ decay

For $\chi_{c1} \to a\pi$ modes we use the $\mathbf{1} \times \mathbf{1}$ rule:

$$\chi_{c1} = \frac{1}{\sqrt{3}}(a^+\pi^- - a^0\pi^0 + a^-\pi^+) \tag{24}$$

For $a \to K\overline{K}$ we use the $\frac{\mathbf{1}}{\mathbf{2}} \times \frac{\mathbf{1}}{\mathbf{2}}$ rules:

$$a^+ = K^+\overline{K}^0, \tag{25}$$

$$a^0 = \frac{1}{\sqrt{2}}(K^+K^- + K^0\overline{K}^0), \tag{26}$$

$$a^- = K^0K^-. \tag{27}$$

Combining Equation 24 with Equations 25-27 we get

$$\chi_{c1}\sqrt{3} = (K^+\overline{K}^0)\pi^- - \frac{1}{\sqrt{2}}\Big[(K^+K^-)\pi^0 + (K^0\overline{K}^0)\pi^0\Big] + (K^0K^-)\pi^+. \tag{28}$$

From Equation 28 we get the ratio of rates:

$$\Gamma(\chi_{c1} \to \pi^+K^-K^0)/\Gamma(\chi_{c1} \to K^+K^-\pi^0) = 2, \tag{29}$$

$$\Gamma(\chi_{c1} \to \pi^-K^+\overline{K}^0)/\Gamma(\chi_{c1} \to K^+K^-\pi^0) = 2, \tag{30}$$

or their sum

$$\Gamma(\chi_{c1} \to \pi^+K^-K^0) + \Gamma(\chi_{c1} \to \pi^-K^+\overline{K}^0) = 4 \cdot \Gamma(\chi_{c1} \to K^+K^-\pi^0). \tag{31}$$

D. Consequences for Dalitz plot analysis

Comparing Equations 21-23 for intermediate states with K^* and Equations 29-31 for intermediate states with $a(980)$, we note that they are identical. Thus observations of $\pi^+K^-K^0$ and charge conjugated $\pi^-K^+\overline{K}^0$ final states on the same Dalitz plot will yield the certain ratio between K^* and $a(980)$ amplitudes for the πKK^0_S Dalitz plot. The same ratio between K^* and $a(980)$ amplitudes is expected for the $K^+K^-\pi^0$ Dalitz plot. This isospin analysis implies that these two Dalitz plots, πKK^0_S and $K^+K^-\pi^0$, can be parametrized using a common set of parameters for each K^* and $a(980)$ intermediate state. From Equations 19, 20 we can write equations between decay amplitudes with K^* mesons

$$\begin{aligned}\text{for } \pi KK^0_S: \quad & a_{K^{*+}K^-\to K^0K\pi} = a_{K^{*-}K^+\to K^0K\pi} = a_{K^{*0}\overline{K}^0\to K^0K\pi} = a_{\overline{K}^{*0}K^0\to K^0K\pi} = \\ \text{for } K^+K^-\pi^0: \quad & = -\frac{1}{\sqrt{2}}a_{K^{*+}K^-\to K^+K^-\pi^0} = -\frac{1}{\sqrt{2}}a_{K^{*-}K^+\to K^+K^-\pi^0}, \end{aligned} \tag{32}$$

where the signs assume equal phases

$$\phi_{K^{*+}} = \phi_{K^{*-}} = \phi_{K^{*0}} = \phi_{\overline{K}^{*0}}. \tag{33}$$

Similar equations between amplitudes with $a_0(980)$ can be obtained from Equation 28

$$\begin{aligned}\text{for } \pi KK^0_S: \quad & a_{a(980)^+\pi^-\to\pi KK^0} = a_{a(980)^-\pi^+\to\pi KK^0} = \\ \text{for } K^+K^-\pi^0: \quad & = -\frac{1}{\sqrt{2}}a_{a(980)^0\pi^0\to K^+K^-\pi^0}, \end{aligned} \tag{34}$$

assuming equal phases

$$\phi_{a(980)^+} = \phi_{a(980)^-} = \phi_{a(980)^0}. \tag{35}$$

Equations 32 and 34 predict that the ratio of amplitudes between these two Dalitz plots is $-\sqrt{2}$. This relative factor does not matter, because each Dalitz plot is normalized separately. In the combined fit we ignore this $-\sqrt{2}$ factor between the amplitudes in the πKK^0_S and $K^+K^-\pi^0$ Dalitz plots, and use common fit parameters for each of K^* mesons and $a_0(980)$ intermediate states

$$a_{K^*} \equiv a_{K^{*+}} = a_{K^{*-}} = a_{K^{*0}} = a_{\overline{K}^{*0}}, \tag{36}$$

$$a_{a(980)} \equiv a_{a(980)^+} = a_{a(980)^-} = a_{a(980)^0}. \tag{37}$$

In Sections VI C and VI B we have checked an isospin symmetry between πKK^0 and $K^+K^-\pi^0$ decays for two particular intermediate states. However, this symmetry is valid independently of how the amplitudes are decomposed into two-body sub-amplitudes, and thus should be valid for all points on the Dalitz plot.

[1] N. Brambilla *et al.*, CERN-2005-005 [hep-ph/0412158] is a comprehensive recent review of heavy quarkonium physics.

[2] Q. Zhao, Phys. Rev. D **72**, 074001 (2005).

[3] S.B. Athar *et al.* (CLEO Collaboration), Phys. Rev. D **70**, 112002 (2004).

[4] M. Ablikim *et al.* (BES Collaboration), Phys. Rev. D **74**, 072001 (2006).

[5] G. Viehhauser *et al.*, Nucl. Instrum. Methods A **462**, 146 (2001).
[6] R.A. Briere *et al.* (CESR-c and CLEO-c Taskforces, CLEO-c Collaboration), Cornell University, LEPP Report No. CLNS 01/1742 (2001) unpublished.
[7] R. Brun *et al.*, Geant 3.21, CERN Program Library Long Writeup W5013 (1993), unpublished.
[8] G.S. Huang *et al.* (CLEO Collaboration), Phys. Rev. Lett. **95**, 181801 (2005); T.E. Coan *et al.* (CLEO Collaboration), Phys. Rev. Lett. **95**, 181802 (2005).
[9] W.M. Yao *et al.*, Journal of Physics G **33**, 1 (2006) (PDG 2006).
[10] V. Filippini, A. Fontana, and A. Rotondi, Phys. Rev. D **51**, 2247 (1995).
[11] S. Kopp *et al.* (CLEO Collaboration), Phys. Rev. D **63**, 092001 (2001).
[12] P. Rubin *et al.* (CLEO Collaboration), Phys. Rev. Lett. **93**, 111801 (2004).
[13] A. Abele *et al.* (Crystal Barrel Collaboration), Phys. Rev. D **57**, 3860 (1998).
[14] J.A. Oller, Phys. Rev. D **71**, 054030 (2005).
[15] B.S. Zou and D.V. Bugg, Eur. Phys. J. A**16**, 537 (2003).